Chapter 6

Relaxor ferroelectricity driven by microscopically off-centered atoms in the macroscopic cubic phase of lead-free $(Ba_{0.92}Ca_{0.08})(Zr_{0.05}Ti_{0.95-x}Sn_x)O_3$; $(0.125 \leq x \leq 0.25)$ system

6.1 Introduction

Perovskite (ABO_3)-based ferroelectrics are characterized by a long-range ordering, which exists between the dipoles caused by an off-centered displacement of the 'B' site cation within the [BO_6] octahedra [19]. Most of the perovskite-based ferroelectrics stabilize into a centrosymmetric cubic phase at high temperatures [19, 55]. The temperature at which the ferroelectric phase of the material transforms into a paraelectric cubic phase is referred to as the Curie temperature (T_c) [19, 55]. The high-temperature cubic phase

of the ferroelectric materials may be tuned in the vicinity of room temperature through chemical substitutions corresponding to 'A' and (or) 'B' sites in order to exploit the exotic properties observed in the vicinity of phase transition temperature [8, 180, 257, 284]. The chemical substitution often leads to a disordered phase, even in the cubic matrix depending on the ionic radii ratio and charge imbalance of the cations (dopants) corresponding to 'A' and (or) 'B' sites [14, 47, 165, 257, 285]. In the chemically (compositional) disordered systems, the different cations arrange themselves at equivalent crystallographic sites in a disordered manner [40]. In many of the studied systems, the disordered phase present in the macroscopic (long-range) cubic matrix comprises the microscopically (short-range) ordered polar clusters known as polar nano-regions (PNRs) [10, 170, 257, 285, 286]. The presence of PNRs in the overall cubic matrix leads to a fascinating class of materials called relaxor ferroelectrics (or relaxors) [39, 41]. The relaxors have been exploited in many applications, such as sensors, electromechanical actuators, energy storage, energy harvesting devices, multilayer ceramic capacitors (MLCCs), etc. [172]. In contrast to normal ferroelectrics, which are characterized by a sharp phase transition temperature termed as Curie temperature (T_c) [19], relaxor ferroelectrics are generally described by a frequency-dependent temperature corresponding to dielectric maxima (T_m) [39]. The existence of a broad phase transition temperature in relaxors is often beneficial since it leads to an increase in the thermal stability of the physical responses of the system making the materials operational over a wide range of temperatures [218, 287]. Among relaxors, the lead-based systems, *viz.,* $Pb(Mg_{1/3}Nb_{2/3})O_3$, $Pb(Zn_{1/3}Nb_{2/3})O_3$, and their solid solutions with $PbTiO_3$ remain essential since they exhibit outstanding application-oriented physical properties [254, 288]. However, the environmental concerns associated with lead-based materials imposed by their toxic nature have intensified the search for lead-free alternatives [34]. In this regard, the highly appealing, technologically important lead-free relaxor ferroelectric materials, *viz.,* $Ba(Zr,Ti)O_3$, $Ba(Sn,Ti)O_3$, are obtained by fabricating the solid

solutions of ferroelectric $BaTiO_3$, with incipient ferroelectric perovskite, *viz.,* $BaZrO_3$, and paraelectric $BaSnO_3$, respectively [46, 47, 145, 289]. In such materials, the T_c decreases with increasing the fraction of $BaZrO_3$ and $BaSnO_3$. Further, the phase transition becomes more and more diffuse, leading to a crossover from normal to relaxor ferroelectrics around 25 and 20 mol% of $BaZrO_3$ and $BaSnO_3$, respectively [8, 46, 47, 180, 289]. In the previous chapter, we have carried out a detailed structure-property correlation study in a similar eco-friendly ceramic system, *viz.,* $(Ba_{0.92}Ca_{0.08})(Zr_{0.05}Ti_{0.95-x}Sn_x)O_3$; BCZTSn$x$ ($0 \leq x \leq 0.10$). The main focus of the study was centered around the analysis of Sn(x) induced various crystallographic phase transitions (driven by component freezing of zone center ferroelectric Γ_4^- soft phonon mode belonging to high symmetry cubic phase with $Pm\bar{3}m$ space group) and their impact on ferroelectric polarization (measured via PE hysteresis loop measurements), which was explained by modifications in amplitudes of the ferroelectric Γ_4^- phonon modes. Moreover, for the composition $x = 0.10$, we have seen that the paraelectric (cubic) to ferroelectric (rhombohedral) phase transition lies at room temperature. In this chapter, we have extended our study for higher Sn content and synthesized the ceramic system BCZTSnx ($0.125 \leq x \leq 0.25$), with all of the compositions having a phase transition lying below room temperature, leading to an average cubic phase at ambient conditions. Further, owing to the presence of $BaSnO_3$-based nonpolar matrix in BCZTSnx ceramics, we have extensively explored the possibility of dielectric relaxor nature for BCZTSnx ($0.125 \leq x \leq 0.25$) system to achieve thermally stable and high physical properties.

6.2 Experimental methods

The samples have been synthesized via a conventional solid-state reaction method. The detailed experimental procedure has been described in chapter 5. To identify the crystallographic phase of the synthesized ceramics, the X-ray diffraction data was collected over the 2θ range 20^o-120^o with a step size of 0.02, using Rigaku MiniFlex 600 X-ray

diffractometer, having Cu-K_α radiation. Further, the crystallographic phase has been fixed by the Rietveld refinements of the diffraction pattern, performed using the FULLPROF package [213]. The temperature-dependent dielectric properties of all the samples at various frequencies (frequency range 10 Hz to 70 kHz) were investigated via Novocontrol impedance analyzer using a closed-cycle refrigerator with a He-gas exchange attachment. The data were collected during the heating cycle at a heating rate of 1 K/min. Further, in order to probe the local structure, the room temperature Raman spectroscopic measurements were carried out over the wavenumber range 50-1000 cm^{-1} using Raman microscope (WiTec alpha 300R, GmbH, Germany) at an excitation wavelength of 532 nm.

6.3 Results and discussions

6.3.1 X-ray diffraction studies

In order to investigate the average structure of various BCZTSnx compositions, the powder diffraction data was preliminarily subjected to peak profile analysis, as in barium titanate-based solid solution, the scrutiny of $\{h00\}$, $\{hh0\}$, and $\{hhh\}$ reflections give an idea about the plausible crystallographic phase(s). Fig. 6.1 depicts the composition-dependent evolution of X-ray diffraction peaks corresponding to (200), (220), and (222) reflections for various compositions. We see that as far as the Sn content is increasing, the peaks shift towards the lower 2θ side due to the replacement of smaller ionic radii Ti^{4+}(61 pm) cations with the larger ionic radii Sn^{4+}(69 pm) cations. Further, the evolution mimics a cubic-like phase for all the compositions since the peaks show a singlet nature. Also, in the previous chapter, we have seen that the increase in Sn content shifts the paraelectric to ferroelectric phase transition of BCZTSnx ceramics towards low temperatures, and for $x = 0.10$, it lies in the vicinity of room temperature. Thus any further increase in Sn(x) content beyond $x = 0.10$ will suppress the paraelectric to ferroelectric phase transition

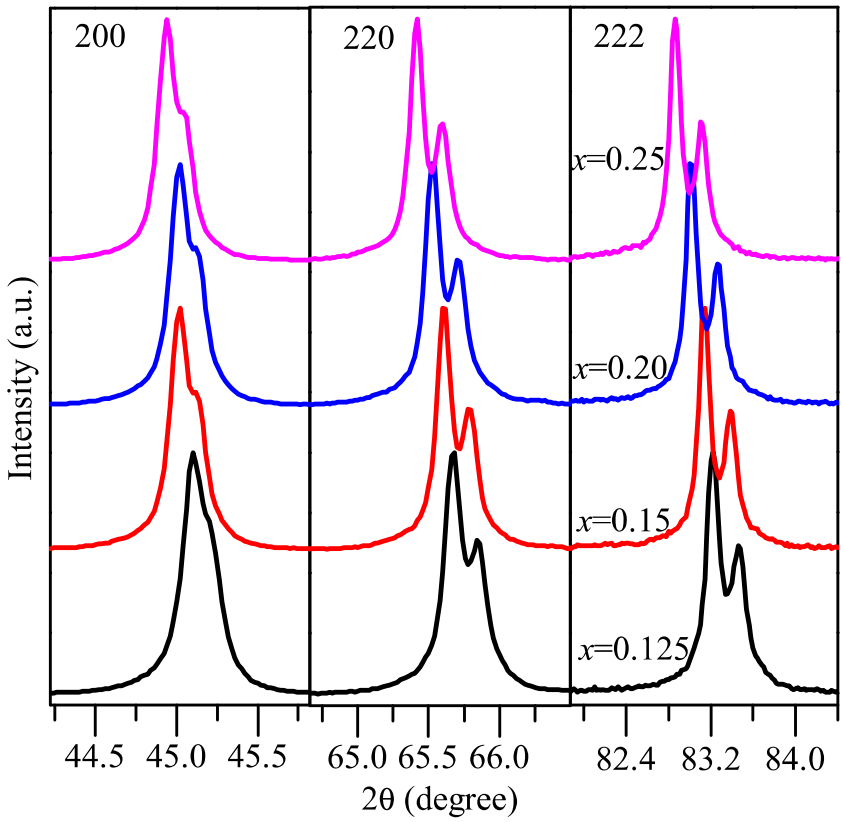

Fig. 6.1 The evolution of 200, 220, and 222, X-ray diffraction peak profiles for BCZTSnx ($0.125 \leq x \leq 0.25$) ceramics.

below room temperature, thereby stabilizing an average cubic phase at room temperature, as also observed in various studies performed in the past [8, 165, 166]. Therefore, to fix the crystallographic structure, we performed the Rietveld refinements using the $Pm\bar{3}m$ space group via FULLPROF software [213]. In the $Pm\bar{3}m$ space group of the cubic phase, Ba/Ca atoms occupy '1a' wyckoff site with positional coordinates (0,0,0), Zr/Ti/Sn atoms occupy '1b' site with positional coordinates ($\frac{1}{2}$,$\frac{1}{2}$,$\frac{1}{2}$), whereas oxygen occupies '3c' site with positional coordinates ($\frac{1}{2}$,0,0). Fig. 6.2 shows the Rietveld refined fits of the diffraction patterns for various compositions. The observed data has been represented by

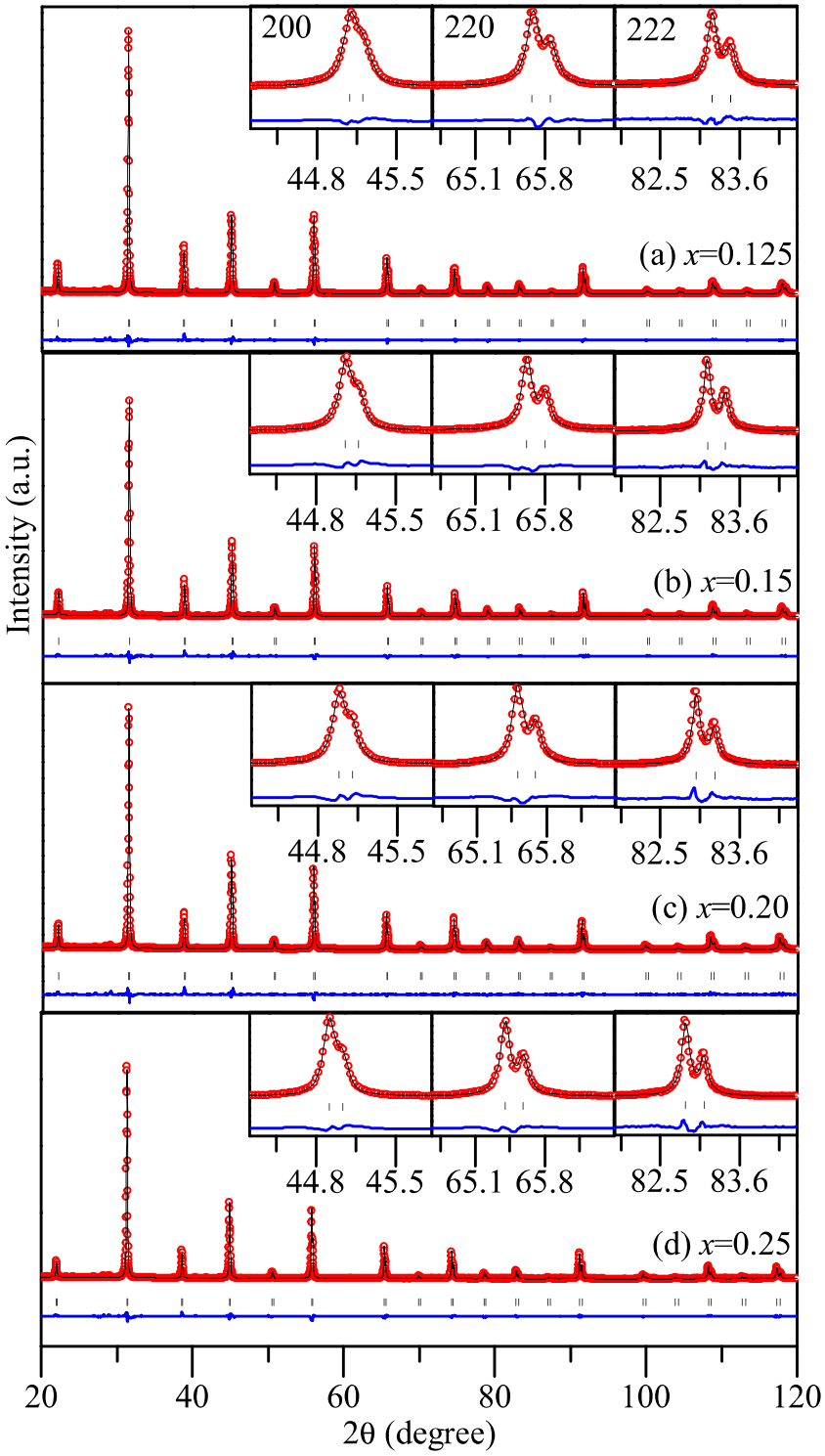

Fig. 6.2 Rietveld fitted X-ray diffraction pattern of BCZTSnx ($0.125 \leq x \leq 0.25$) ceramics via cubic phase having $Pm\bar{3}m$ space group.

Table 6.1 Structural parameters and various agreement factors obtained from Rietveld refinements of room temperature X-ray diffraction data of BCZTSnx ($0.125 \leq x \leq 0.25$) ceramics via cubic ($Pm\bar{3}m$) phase.

structural	composition (x)			
parameters	$x = 0.125$	$x = 0.15$	$x = 0.20$	$x = 0.25$
a(Å)	4.018117(17)	4.02080(3)	4.02689(3)	4.03275(5)
V(Å^3)	64.8736(5)	65.0037(7)	65.2995(8)	65.5848(14)
Ba/Ca [U(Å^2)]	0.00550(18)	0.00678(18)	0.00760(19)	0.0076(2)
Zr/Ti/Sn [U(Å^2)]	0.0077(3)	0.0084(3)	0.0084(3)	0.0086(3)
O [U(Å^2)]	0.0052(6)	0.0032(6)	0.0033(7)	0.0042(8)
χ^2	10.6	12.4	13.9	12.1
R_{wp}	7.49	8.04	8.45	7.96
R_{exp}	2.30	2.28	2.26	2.29

open red circles, while continuous black lines represent the simulated diffraction pattern. The vertical gray lines show the Bragg reflections, while the horizontal blue line below the vertical bar corresponds to the difference between the observed and simulated diffraction patterns. The fit obtained with the cubic $Pm\bar{3}m$ model is satisfactory for all the compositions, and the obtained values of the various agreement factors are also found to be quite reasonable (see Table 6.1). In order to show the quality of Rietveld fitting, the magnified view of the fitted peaks corresponding to (200), (220), and (222) reflections have also been shown in the inset of Fig. 6.2. Thus, our X-ray diffraction analysis concludes an average cubic ($Pm\bar{3}m$) phase for all the BCZTSnx ($0.125 \leq x \leq 0.25$) compositions.

6.3.2 Dielectric studies

Fig. 6.3 shows the temperature-dependent variation of the real and imaginary part of the dielectric permittivity for BCZTSnx ceramics, measured at various frequencies ranging between 10 Hz to 70 kHz. The dielectric permittivity maxima clearly show a broadened nature. Also, the temperature corresponding to dielectric maxima, *i.e.,* $T = T_m$, exhibits a frequency dependence, and its value increases with an increase in frequency for the compositions $0.15 \leq x \leq 0.25$ (see inset in Fig. 6.3), dictating the presence of a relaxor

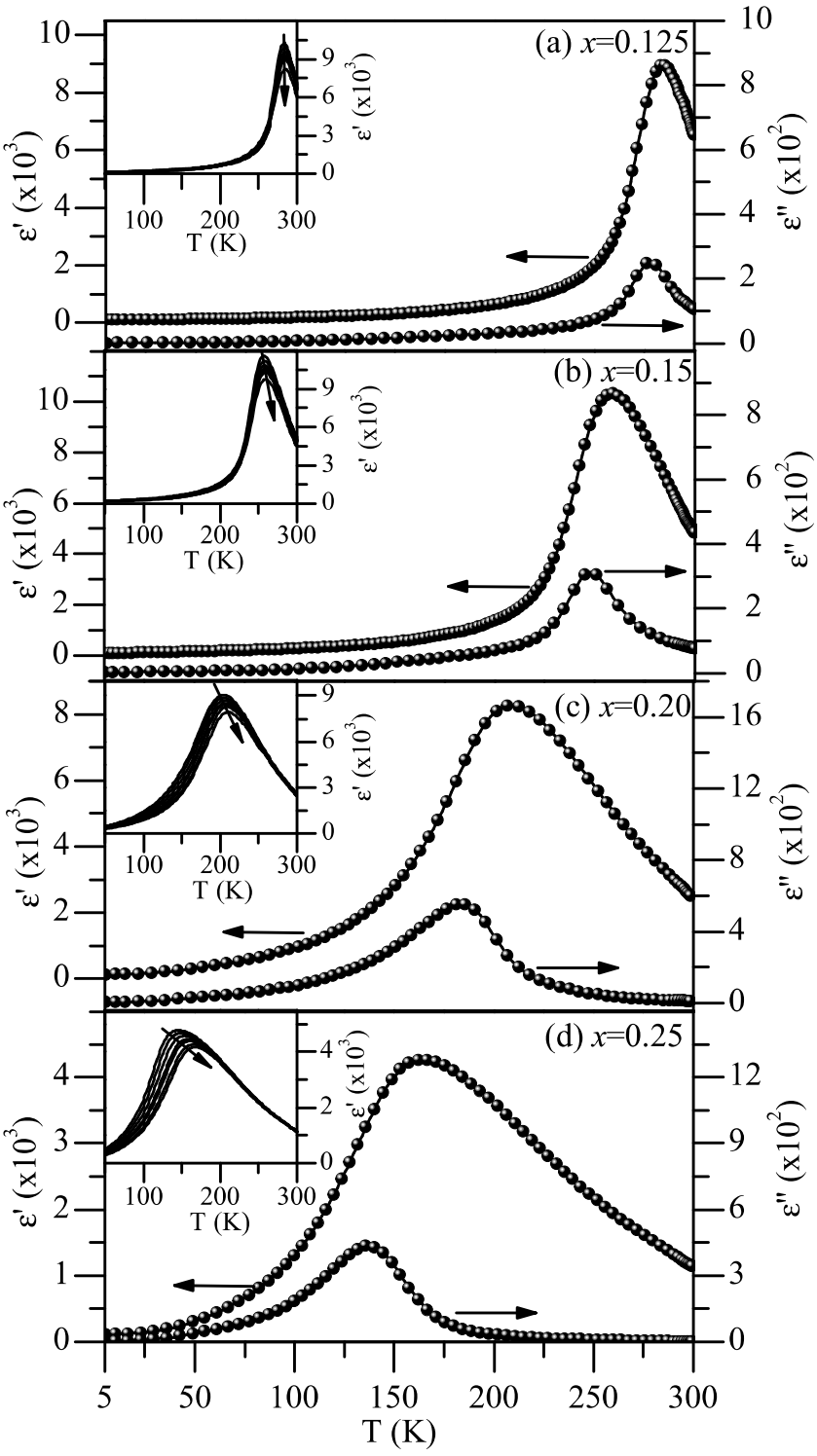

Fig. 6.3 Temperature-dependence of real (ε') and imaginary (ε'') part of dielectric permittivity for BCZTSnx ($0.125 \leq x \leq 0.25$) ceramics at 30 kHz .

ferroelectric behaviour [40, 290]. In addition, the peak observed in the imaginary part of the dielectric permittivity corresponds to lower temperatures in comparison with the temperature corresponding to the peak value of the real part of dielectric permittivity, and a significant difference between the two maxima can be seen except for $x = 0.125$, where the peaks lie approximately at the same value. Moreover, the difference between the temperatures corresponding to the real and imaginary part of the dielectric maxima increases with the increase in Sn(x) content (see Fig. 6.3). The existence of this feature further corroborates the relaxor ferroelectric behaviour [40, 134, 290, 291], for the compositions $0.15 \leq x \leq 0.25$.

It is very well accepted that normal ferroelectrics obey the Curie-Weiss law for $T > T_m$ [19, 21],

$$\frac{1}{\varepsilon'} = \frac{(T - T_{cw})}{C} \tag{6.1}$$

where T_{cw} is the Curie-Weiss temperature, and C stands for Curie-Weiss constant. The Curie-Weiss law also holds for relaxor ferroelectrics but far above the temperature corresponding to the dielectric maxima (T_m) termed as Burn's temperature, below which a deviation from Curie-Weiss law occurs. In relaxor ferroelectrics, such a deviation occurs due to the appearance of short-range dipole-dipole interactions in contrast to long-range ordered ferroelectric state. It is generally believed that, above the Burn's temperature, the phase exhibits paraelectric behaviour with no PNRs, and has an average cubic structure similar to the high-temperature cubic phase of normal ferroelectrics. Upon cooling, the dynamical PNRs start appearing in the macroscopic cubic matrix. The local dynamical PNRs start appearing at Burn's temperature, leading to the formation of an ergodic relaxor state [138, 292].

To get insight into the nature of short-range dipolar correlations, the dielectric permittivity *vs.* temperature curve was fitted using the modified Curie-Weiss law given below [143, 144, 290],

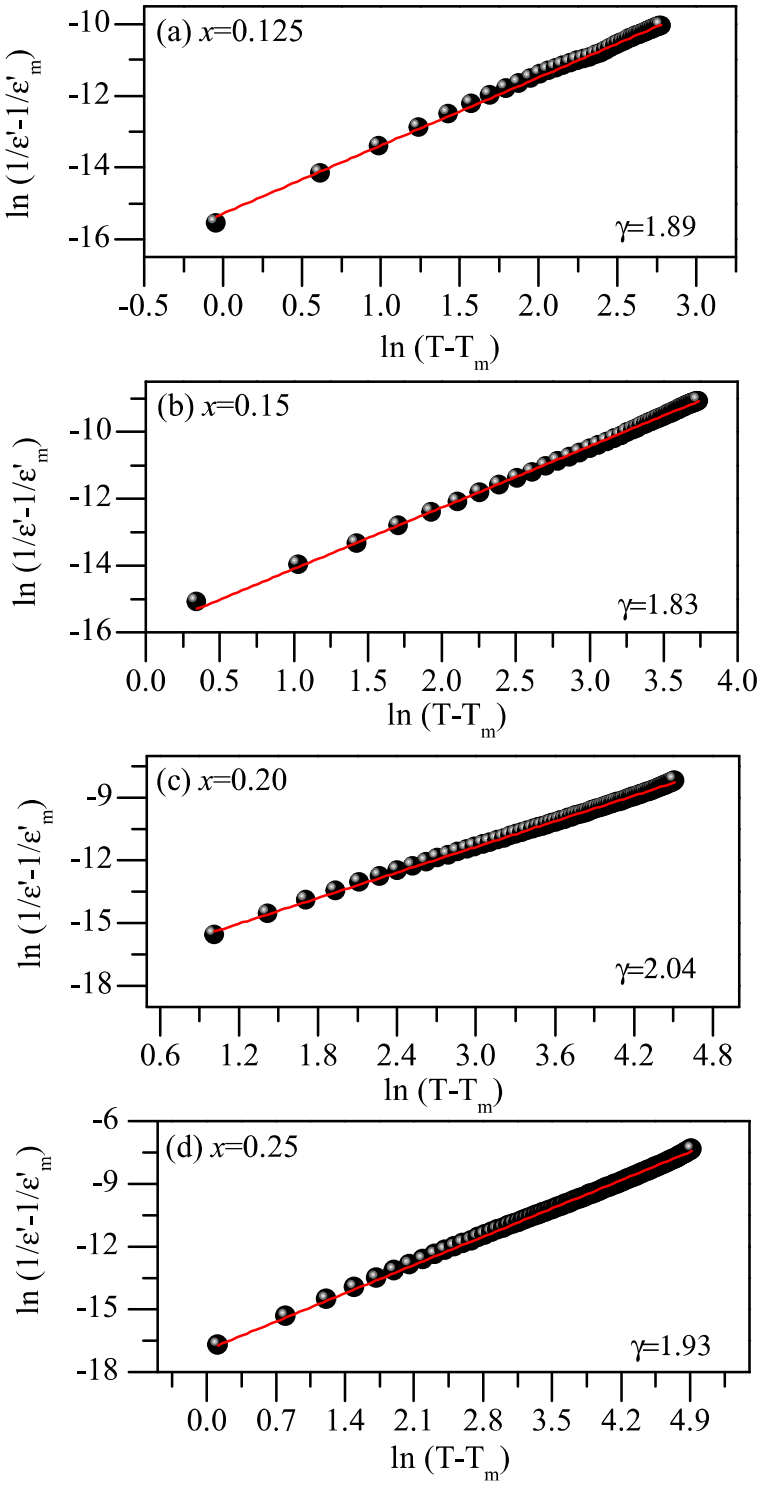

Fig. 6.4 The linear fitting of ln $(\frac{1}{\varepsilon'} - \frac{1}{\varepsilon_m})$ *vs.* ln ($T-T_m$) plot for BCZTSnx ($0.125 \leq x \leq 0.25$) ceramics at 30 kHz.

$$\frac{1}{\varepsilon'} - \frac{1}{\varepsilon'_{\mathrm{m}}} = \frac{(T - T_{\mathrm{m}})^{\gamma}}{C}; T > T_{\mathrm{m}} \tag{6.2}$$

where, $\varepsilon'_{\mathrm{m}}$ is the value of dielectric permittivity corresponding to T_{m}, and γ is called the diffusion exponent whose value lies between $1 \leq \gamma \leq 2$. The limiting values, *i.e.,* γ = 1, characterizes an ideal ferroelectric, whereas γ = 2 corresponds to an ideal relaxor ferroelectric [144]. The γ values obtained by fitting the ln $(\frac{1}{\varepsilon'} - \frac{1}{\varepsilon_{\mathrm{m}}})$ *vs.* ln (T-T_{m}) data using modified Curie-Weiss law, are 1.89 (x = 0.125), 1.83 (x = 0.15), 2.04 (x = 0.20), and 1.93 (x = 0.25). These values of γ are close to the relaxor ferroelectrics. However, the γ values don't show a systematic behaviour as a function of Sn(x). Here, it is worth mentioning that the γ values have been calculated by performing the linear fitting (see Fig. 6.4) and may vary for the different regions of the curve, making the results ambiguous. Moreover, for one of the compositions (x = 0.20), the γ value was greater than two (limiting value corresponding to relaxors). In the previous studies, also, the γ values greater than two have been observed, which makes the interpretation of the results ambiguous [293, 294]. In addition, for Ba(Zr,Ti)O_3 ceramics, it has been observed that although the relaxor nature was increasing with the increase in Zr content but the value of γ was not systematically increasing [293], similar to what has been observed in our studies for BCZTSnx ceramics. Furthermore, the calculation of γ involves only the T>T_{m} region of the dielectric permittivity *vs.* temperature plot, but the diffuseness of the phase transition is associated with a wide region of dielectric permittivity *vs.* temperature plot including both the T>T_{m} as well as T<T_{m} regions. Thus γ can not be considered as an appropriate parameter to quantify the diffuseness of the phase transitions having a broad peak in the dielectric permittivity *vs.* temperature plot [236, 293].

Therefore, in order to have a clear insight into the diffuse nature of phase transitions, another parameter termed as diffuseness degree (D) has been used, which is defined as [236],

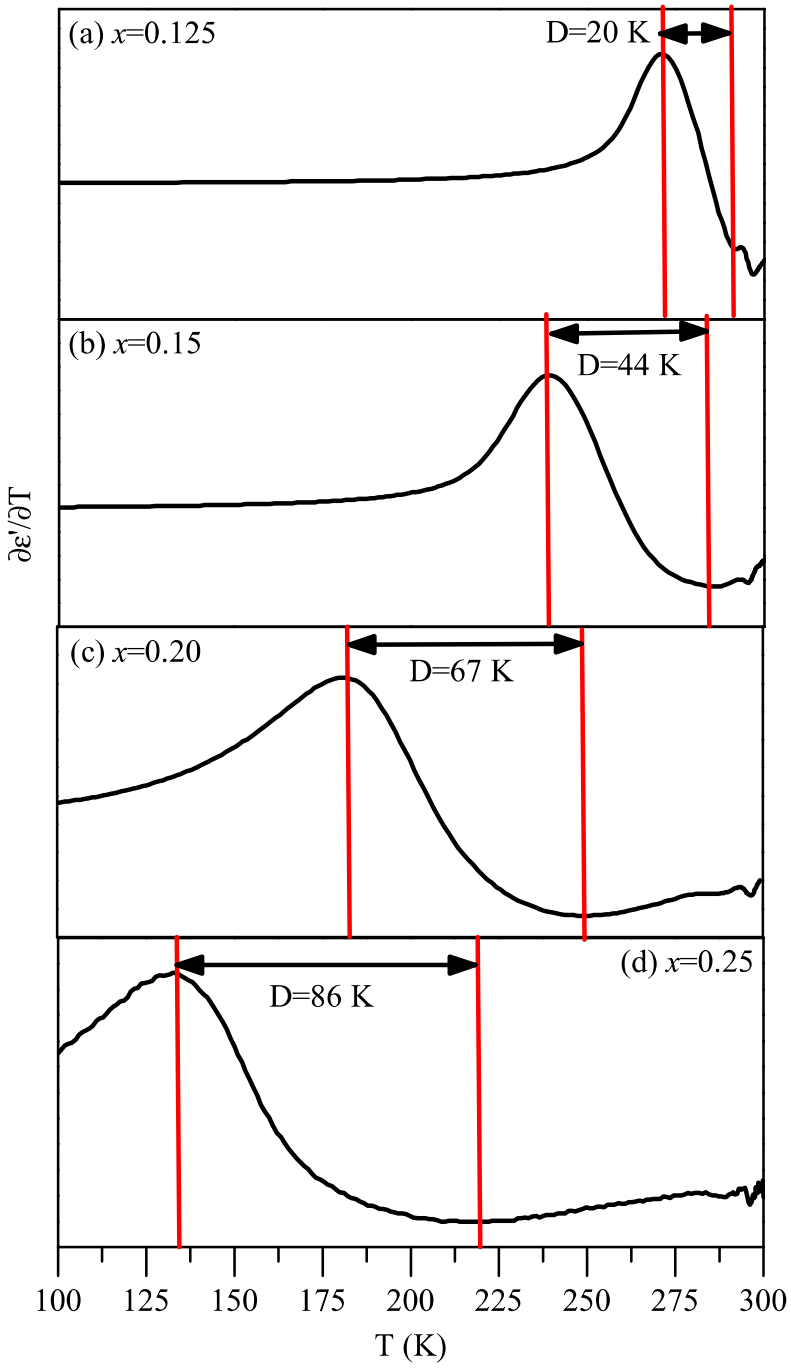

Fig. 6.5 The variation of $\frac{\partial \varepsilon'(T)}{\partial T}$ *vs.* temperature (T) for BCZTSnx ($0.125 \leq x \leq 0.25$) ceramics at 30 kHz.

$$D = T_{(\frac{\partial \varepsilon'(T)}{\partial T} min)} - T_{(\frac{\partial \varepsilon'(T)}{\partial T} max)} \tag{6.3}$$

where $T_{(\frac{\partial \varepsilon'(T)}{\partial T} min)}$ and $T_{(\frac{\partial \varepsilon'(T)}{\partial T} max)}$ are the temperatures corresponding to the minimum and maximum value of $\frac{\partial \varepsilon'(T)}{\partial T}$, respectively. The previous studies demonstrate that the variation of dielectric permittivity ε'(T) with temperature (T) in relaxors is governed by the microscopic polar regions, which leads to the dielectric relaxational phenomenon. Therefore the temperature interval of the extrema of $(\frac{\partial \varepsilon'(T)}{\partial T})$ will give rise to the diffuseness degree of ε'(T) *vs.* T curve. These two points, *viz.*, $T_{(\frac{\partial \varepsilon'(T)}{\partial T} min)}$ and $T_{(\frac{\partial \varepsilon'(T)}{\partial T} max)}$ correspond to the temperature where the dielectric permittivity of the material shows the most rapid change due to the presence of microscopic polar regions [236]. The D value predicts clearly the behaviour of the diffuse nature of phase transitions as it covers both the $T \geq T_m$ and $T \leq T_m$ regions of the ε' *vs.* T curve and thus very well reflects the fundamental characteristics of the diffuse phase transition [236]. Further, its unit is of the temperature, which makes it more meaningful while characterizing the diffuseness of phase transition [236]. The calculated value of D ranges between 20 K$\leq$ T $\leq$ 86 K for $0.125 \leq x \leq 0.25$ with an increasing trend, indicating that the transitions become more diffuse with the increase in Sn(x) content.

6.3.3 Raman spectroscopic studies

In order to further analyse the nature of short-range atomic ordering in the average cubic matrix, we have performed the composition-dependent Raman spectroscopic measurements of BCZTSnx ceramics. The Sn doping leads to the compositional disorder resulting in the broadening of the Raman peaks, which makes difficult to unequivocally assign the various modes. Therefore, we have performed the deconvolution of the Raman spectra via Lorentz fitting of the broad peaks. The Raman spectra of the cubic phase of the parent $BaTiO_3$ is characterized by two broad peaks situated around 275 cm^{-1} and 514 cm^{-1}, having an asymmetric nature [204, 262], but our composition-dependent Raman spectroscopic

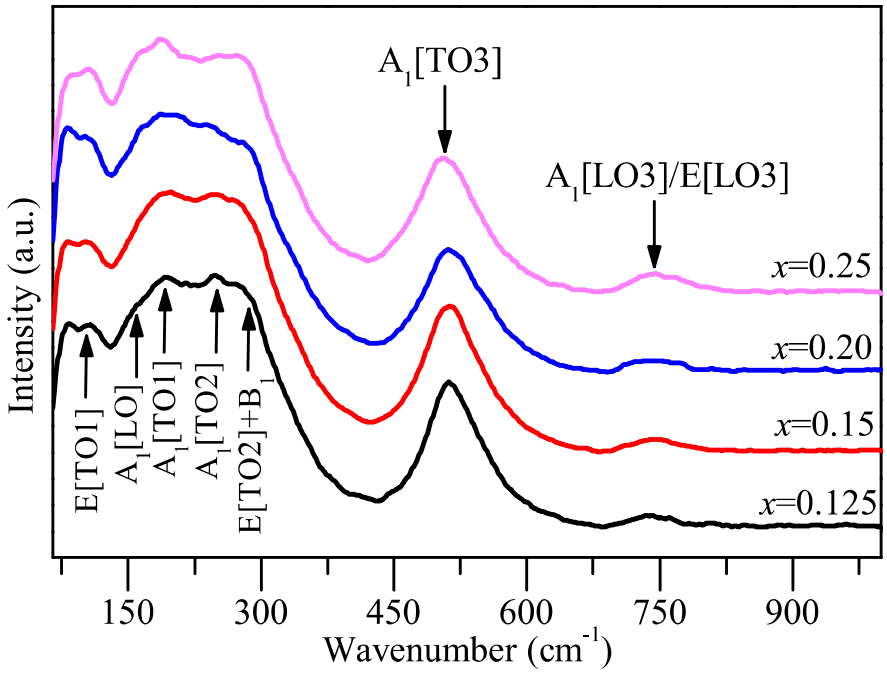

Fig. 6.6 Room temperature Raman spectra of BCZTSnx ($0.125 \leq x \leq 0.25$) ceramics.

measurements show various other peaks in contrast to those observed in the cubic phase. Since our X-ray diffraction analysis has inferred a simple cubic phase for all the BCZTSnx ceramics, in contrast to the observations made via Raman spectroscopic measurements, it becomes worth mentioning that the X-ray diffraction is an average structural determination technique; therefore, the observed features in the Raman spectra will be associated with the local level structural modifications present in the material. These modifications appear in the Raman spectra due to its capability to detect atomic arrangements existing over a few unit cells [225, 226, 227]. The deconvolution of the peaks shows that the observed Raman spectra for all the compositions correspond to the low-temperature rhombohedral phase of barium titanate [204], despite having an average cubic phase for all the compositions inferred by X-ray diffraction studies. Therefore, the Raman spectra reveals the presence of rhombohedral-like short-range ordering in the average cubic matrix. The deconvolution of the Raman spectra reveals the presence of various modes, *viz.,* E[TO1], A_1[LO], A_1[TO1],

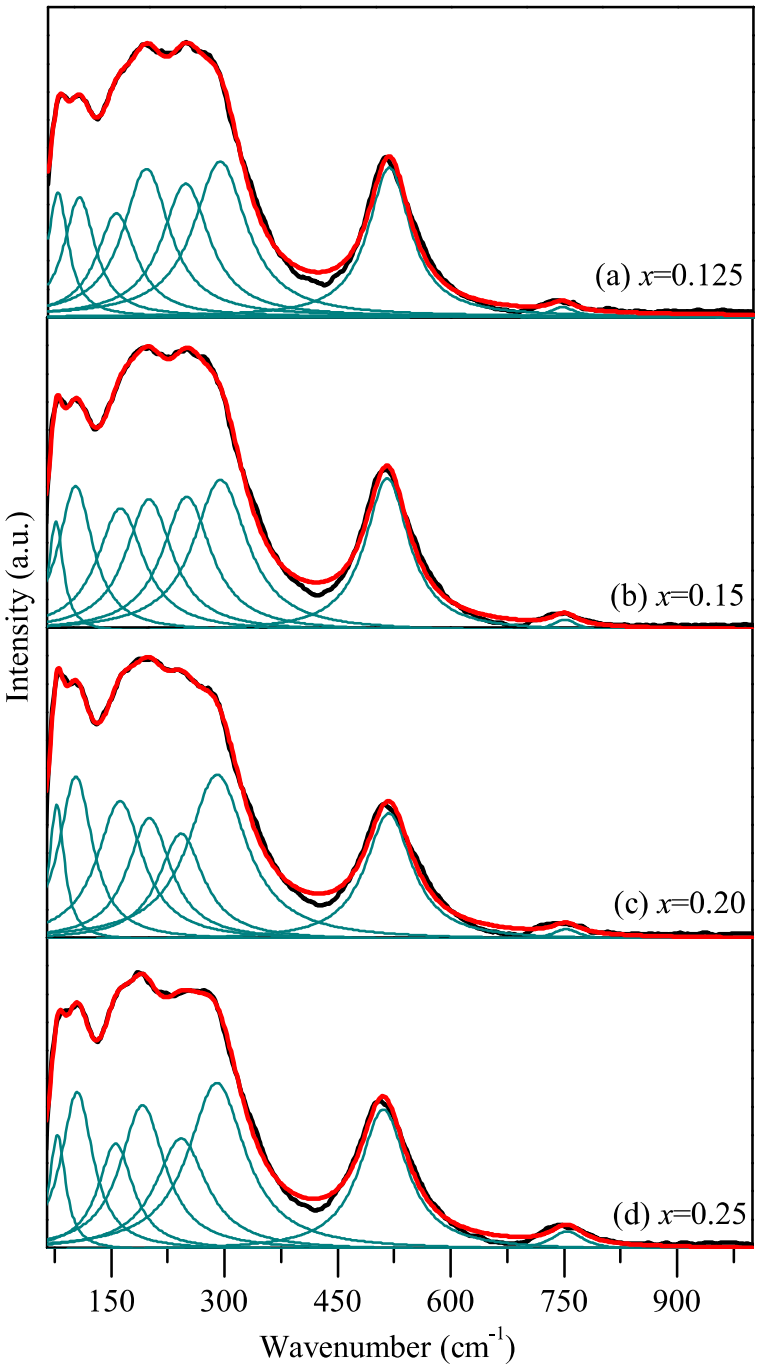

Fig. 6.7 The peak fitting of the Raman spectra for BCZTSnx ($0.125 \leq x \leq 0.25$) ceramics.

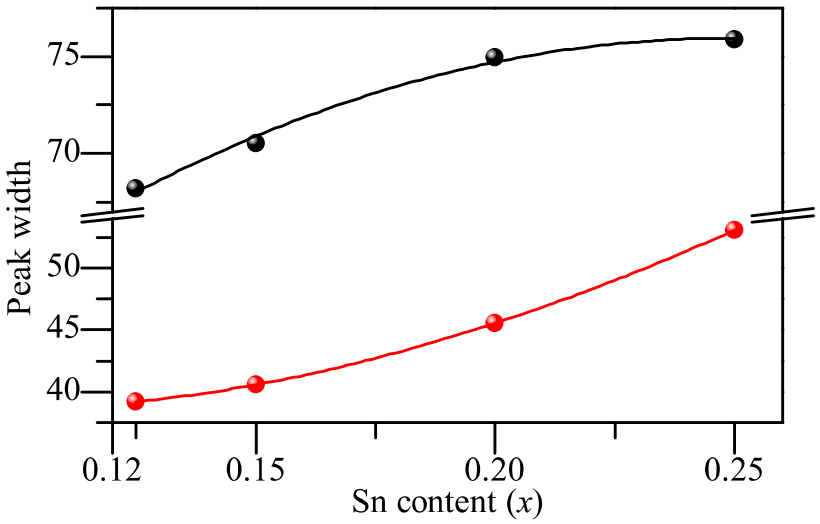

Fig. 6.8 Variation in peak width corresponding to 512 cm^{-1} (black dots), and 747 cm^{-1} (red dots) mode for BCZTSnx ($0.125 \leq x \leq 0.25$) ceramics.

A_1[TO2], E[TO2]+B_1, A_1[TO3], and A_1[LO3]/E[LO3]. The presence of different TO excitations reveals the presence of ferroelectric-like distortions, despite having a macroscopic cubic structure inferred from X-ray diffraction studies [249]. The E[TO1] mode present around 106 cm^{-1} indicates the presence of Sn and Zr-based clusters having a local rhombohedral structure [189, 227, 238, 242]. This peak arises when the Sn and Zr rich regions are around tens of unit cells in size, allowing the phonons to produce a definite Raman spectrum [189, 227]. Along with these modes, a dip appears around 129 cm^{-1} due to the coupling between the A_1[TO1] and A_1[TO2] phonon modes resulting due to the difference in the ionic radii of the 'B' site cation in [BO_6] octahedra [262, 263]. In literature, this peak has been assigned to the polar nano-regions resulting due to breaking of long-range ferroelectric ordering of [TiO_6] octahedra by the substitution of Sn and Zr with larger ionic radii at 'B' site making the respective unit cells nonpolar [262, 263]. The substitution of smaller Ti^{4+} (61 pm) cations by larger Sn^{4+} (69 pm) cations leads to a random stress field, which effectively disrupts the long-range correlated O-Ti-O chain, resulting in the relaxor ferroelectric behaviour. Furthermore, the peak around 512 cm^{-1}

corresponds to A_1[TO3] mode and is associated with the concentration of polar [TiO_6] octahedra in the cubic matrix [248]. The fitting of the corresponding peak in the Raman spectra (see Fig. 6.7) shows an increase in the width of the peak with increase in Sn content (see Fig. 6.8), indicating an increase in the structural disorder as a function of Sn(x). Earlier, the studies performed by Margaritescu *et al.* demonstrated the disappearance of LO modes in the absence of ferroelectric ordering, but one can see the presence of A_1[LO3]/E[LO3] modes for all compositions, indicating the presence of sufficient electrostatic field even in the macroscopically cubic phase revealing the ferrolectric-like local disorder in the cubic matrix [249]. Veselinovic *et al.* associated the A_1[LO3]/E[LO3] modes in the Sn-doped $BaTiO_3$ system, with the distorted polar [TiO_6] clusters existing in the macroscopic cubic matrix [165]. It can be seen from Fig. 6.6 that the broadening of the peak corresponding to A_1[LO3]/E[LO3] mode is increasing with the Sn(x) content (see Fig. 6.8), which is further attributed to the increase of disorder in [TiO_6] octahedra.

We have seen, therefore, that the dielectric relaxational behaviour in BCZTSnx ceramics increases with increase in Sn(x) content. Let us now discuss the possible mechanism behind such trend and the origin of PNRs that leads to relaxor behaviour. For a long time, the presence of charge disorder (arrived due to the chemical inhomogeneity) has been considered as an essential requirement for the formation of polar nano-regions. Earlier, the diffuse phase transition in $Pb(Mg_{1/3}Nb_{2/3})O_3$ was considered to appear due to the fluctuations in random-internal-electric-fields caused by the quenched charge disorder, where the same crystallographic positions are randomly occupied by the cations with different valencies [41, 152, 295]. These random electric fields prevent the formation of a long-range ordered ferroelectric state resulting into a disordered polar nano-domain state. However, in solid solutions such as Ba(Zr,Ti)O_3, and Ba(Sn,Ti)O_3, no charge disorder can be expected because of the homovalent nature of the cations corresponding to 'B' sites. Thus such substitutions will not be able to give rise to quenched random

electric field held responsible for relaxor ferroelectricity in $Pb(Mg_{1/3}Nb_{2/3})O_3$. In order to explain the origin of relaxor ferroelectricity in homovalent ceramics, *viz.,* $Ba(Zr,Ti)O_3$, and $Ba(Sn,Ti)O_3$, the model has been proposed by Kleeman [295]. The observed local random displacements of the ferroelectrically active Ti^{4+} cations in the relaxor ferroelectric state of the above-mentioned homovalent solid solutions are caused by the quenched random-internal-stress-field generated by the random distributions of the Zr^{4+}/Sn^{4+} cations having significantly larger ionic radii than Ti^{4+} cations. These random-internal-stress-fields effectively disrupt the long-range correlated O-Ti-O chain, and results in a relaxor ferroelectric behaviour [135, 295].

Also, the explored ceramic system, *i.e.,* BCZTSn*x*, has been derived from the well-known ferroelectric $BaTiO_3$. In normal ferroelectric such as $BaTiO_3$, every unit cell has the dipoles formed by the off-centered displacements of the $B(Ti^{4+})$ site cations within the octahedral cage made by the oxygen atoms. These off-centered displacements of $B(Ti^{4+})$ site cations appear due to a covalent character of Ti-O bonds, which is governed by a strong hybridization between the $3d$ electronic states of the Ti^{4+} cations and the $2p$ states of O^{2-} anions. The presence of a strong hybridization reduces the short-range repulsion and leads to dipole-dipole interactions, which builds up the spontaneous polarization in $BaTiO_3$. Here, it is worth mentioning that short-range repulsions are the forces that try to stabilize the centrosymmetric phase [16]. Therefore, the balance between short-range repulsions, which favour a non-ferroelectric phase, and bonding considerations, which favours the ferroelectric phase, determines whether a centrosymmetric (non-ferroelectric) or non-centrosymmetric (ferroelectric) phase will stabilise. The first principle calculations performed by Shi *et al.* on $Ba(Sn,Ti)O_3$ system demonstrate a significantly less overlap between the Sn and oxygen atoms in comparison to Ti and oxygen atoms [9]. This indicates that the orbital hybridization between Sn and O atoms becomes much weaker than the one present between Ti and oxygen atoms. Therefore, the dipole can barely occur in the unit

cells where Ti atoms have been replaced by Sn. Thus, the long-range ordering between the dipoles will be disrupted in the areas of the matrix where the concentration of Sn atoms is sufficiently high [9]. Therefore in BCZTSnx ceramics, it is reasonable to believe that the increase of non-ferroelectric environment in the ferroelectric matrix is a prominent reason for the existence of short-range ordering in the cubic matrix.

6.4 Conclusion

In conclusion, we observed the presence of short-range ferroelectric ordering in the average cubic ($Pm\bar{3}m$) phase of BCZTSnx ($0.125 \leq x \leq 0.25$) ceramics. Further, the nature of short-range ordering for $0.125 \leq x \leq 0.25$, as inferred from Raman spectroscopic studies, is consistent with the low-temperature rhombohedral symmetry of barium titanate. As a consequence of short-range ordering driven polar nano-regions in the cubic matrix, all the compositions exhibit a broad peak in dielectric permittivity *vs.* temperature plot with a non-relaxor nature for $x = 0.125$, which transforms into a relaxor ferroelectric for $x = 0.15$. Moreover, as far as Sn content increases, the dielectric relaxational behaviour increases. Owing to the presence of a high dielectric constant with a relaxor ferroelectric nature, these ceramics can act as a potential candidate for various energy storage applications.

In the next chapter, we have presented a brief conclusion and suggestions regarding future works related to this thesis.